Spatial organization and correlation properties quantify structural changes on mesoscale of parenchymatous plant tissue

N. A. Valous,[1] A. Delgado,[1] K. Drakakis,[2] and D.-W. Sun[1,a)]
[1]*School of Biosystems Engineering, University College Dublin, National University of Ireland, Belfield, Dublin 4, Dublin, Ireland*
[2]*Complex & Adaptive Systems Laboratory, University College Dublin, National University of Ireland, Belfield, Dublin 4, Dublin, Ireland*

(Received 25 November 2013; accepted 7 January 2014; published online 10 February 2014)

The study of plant tissue parenchyma's intercellular air spaces contributes to the understanding of anatomy and physiology. This is challenging due to difficulty in making direct measurements of the pore space and the complex mosaic of parenchymatous tissue. The architectural complexity of pore space has shown that single geometrical measurements are not sufficient for characterization. The inhomogeneity of distribution depends not only on the percentage content of phase, but also on how the phase fills the space. The lacunarity morphometric, as multiscale measure, provides information about the distribution of gaps that correspond to degree of spatial organization in parenchyma. Additionally, modern theories have suggested strategies, where the focus has shifted from the study of averages and histograms to the study of patterns in data fluctuations. Detrended fluctuation analysis provides information on the correlation properties of the parenchyma at different spatial scales. The aim is to quantify (with the aid of the aforementioned metrics), the mesostructural changes—that occur from one cycle of freezing and thawing—in the void phase of pome fruit parenchymatous tissue, acquired with X-ray microcomputed tomography. Complex systems methods provide numerical indices and detailed insights regarding the freezing-induced modifications upon the arrangement of cells and voids. These structural changes have the potential to lead to physiological disorders. The work can further stimulate interest for the analysis of internal plant tissue structures coupled with other physico-chemical processes or phenomena.
 [http://dx.doi.org/10.1063/1.4862641]

I. INTRODUCTION

The apple fruit cortex is mainly composed of the fleshy tissue of parenchyma cells permeated with vascular tissue and intercellular air spaces.[1] Parenchyma cell walls have a thin primary layer, with randomly distributed cellulose fibres reinforcing a matrix of hemicellulose, pectin, and glycoproteins.[2] The nanostructure of the cell walls differs for different apple cultivars in terms of cellulose diameter, crystallinity, and pectin content.[3] The cells immediately beneath the surface are small (approx. 50 μm), rounded, and randomly orientated. Progressing towards the center, there is a gradual increase in cell size until they reach a maximum diameter (approx. 200–250 μm) at approx. 5 mm from the surface. Cell size is not only determined genetically but also by the environment, crop load, and maturity.[4] The voids between apple parenchyma form an incompletely connected network; void spaces can be long and may stretch over several hundreds of μm in the tissue. These voids do not connect or split, but are surrounded by smaller individual voids without preferential direction.[5] Parenchyma cells may assume distinctive characteristics by accumulating specific kinds of substances, i.e., apple parenchyma cells store carbohydrates.[6] The study of parenchyma's intercellular air spaces has important applications since they are related to the understanding of anatomy and physiology.[7] Quantification may be challenging due to the difficulty in making direct measurements of the pore space and the complex anisotropic mosaic of the parenchyma tissue.[8] The first issue can be solved with X-ray μCT (micro-computed tomography), which determines reliably the architecture of opaque porous media at μm to sub-μm resolutions.[9,10] The second issue can be tackled by measuring the spatial organization and correlation properties of tissue patterns.

Spatial patterns may exhibit scale-dependent changes in structure and often are difficult to identify and describe.[11] Lacunarity, as a second order statistical measure, quantifies the relationship between neighboring objects/pixels,[12] explicitly characterizes spatial organization, and quantifies the degree of translational invariance.[13,14] It uses multiscale windowing for measuring the scale dependency of heterogeneity, thus characterizing the geometry of deterministic and random sets.[15] In essence, it measures how data fill the space,[16] enabling the parsimonious analyses of patterns: aspects of gaps distribution, presence of structures, homogeneity in gaps distribution, and random or self-similar behavior.[17] Lacunarity is sensitive to local aggregation or clustering and handles departures from stationarity.[18] In principle, lacunarity may seem similar to the concept of multifractals.[19] However, multifractals discern a globally consistent value based upon the singularity of local scaling exponents, whereas lacunarity defines the magnitude of local variations not as they scale outward from those localities, but rather between localities.[20]

a)Author to whom correspondence should be addressed. Electronic mail: dawen.sun@ucd.ie. Fax: +353 (0)1 7167493.

In addition, patterns can be analyzed through their correlation properties. Persistent and anti-persistent correlations are collectively called long memory or long-range dependence,[21] which is characterized by a hyperbolically decaying autocovariance function, by a spectral density that tends to infinity as the frequencies tend to zero, and by the self-similarity of aggregated summands.[22] Assessing its strength is accomplished using the Hurst exponent (H), which is a numerical predictability estimate; $H \neq 0.5$ indicates memory or auto-correlation in the sequence, while $H = 0.5$ produces conventional Brownian motion.[23] In a persistent process ($H > 0.5$), large values tend to follow large values and small values tend to follow small values. The strength of persistence increases as $H \rightarrow 1.0$.[24] In an anti-persistent process ($H < 0.5$), large and small values tend to alternate.[25] If series extracted from images are driven by non-stationarities—which are usually the case—Hurst exponents are highly likely to be biased.[26] Detrended fluctuation analysis (DFA)[27] is a modified root-mean-square analysis of a random walk[28] that provides a measure of the fluctuations in non-stationary series and the presence or absence of correlation properties.[29]

Freezing,[112–115] like Cooling,[116–119] drying[120–124] and edible coating[125] are common techniques used to maintain the quality of agri-food products. For pome fruit tissue, freezing affects its functional and mechanical characteristics.[30] Structural changes have the potential to lead to physiological disorders.[5] The structural modifications due to freezing can be assessed at a number of length scales. Lacunarity and DFA should be able to register such changes quite effectively at the level of the mesoscale. The significance of these metrics for characterization stems from the fact that they can provide numerical indices about the structural variability of parenchyma tissue over a multiscale range. The objective is to quantify the mesostructural changes in the intercellular air spaces of frozen-thawed pome fruit parenchymatous tissue. The quantification of the aforementioned meso-architectural descriptors is carried out on two-dimensional (2D) sections that are obtained from the three-dimensional (3D) organization of cells and voids in the parenchyma tissue. Images representing pores and solids are often used for providing quantifiable information using methods that are sensitive to the spatial arrangement of pores.[31]

II. EXPERIMENTAL SETUP

A. Toolset

Algorithms and analyses are prepared using MATLAB R2011b (Mathworks, USA). The code for computing lacunarity is developed using the gliding-box methodology.[11] The code for computing DFA[32] is adapted for images[26] and then vectorized for computational efficiency. SigmaPlot v12 (Systat Software, USA) is used to perform nonlinear data fitting, Spearman's rank correlations, and Kruskal-Wallis analysis of variance on ranks with post-hoc pairwise multiple comparisons using Tukey's honest significance test (p-values < 0.05 are considered statistically significant). The first derivatives of lacunarity and DFA curves are obtained using a pseudo second-order accurate numerical scheme; this returns dy/dx having the same size as y, handles unequally spaced data, and features accurate treatment for end-points. For DFA—before computing dy/dx—piecewise polynomial fitting is carried out; this has advantages over high degree polynomials, since it allows polynomial degree to be kept low and provides flexibility by making use of a sufficient number of segments joined in a smooth way.[33] The stationarity of rows and columns of the 8-bit images (used in DFA) is assessed using the Kwiatkowski–Phillips–Schmidt–Shin (KPSS) test.[34]

B. Image acquisition and processing

Cylinders from cortex tissue (*Malus domestica* Borkh. cv Granny Smith; 86.9% w/w moisture content, soluble solids content $\approx 12^{\circ}$ Brix) are cut using a cork borer (diameter: 1.8 cm, height: 2.5 cm) in radial orientation from the middle parenchyma (approx. 10 mm from skin). Freezing is completed when temperature reaches $-18\,^{\circ}$C at the center of the cylinders (measured with a type T thermocouple). Three apple cylinders are selected for imaging; a control noted as fresh (FH), and two frozen-thawed samples (FN1 and FN2, collectively noted as FN). The three cylinders are scanned with a Scanco micro-CT40 scanner (Scanco Medical AG, Switzerland) at a linear resolution of 10 μm/pixel, operating voltage of 70 kV, current of 114 mA, and exposure time of 8.4 s. A stack of 200 cross-sectional 8-bit (grayscale) images (2048×2048 pixels) per cylinder is obtained. Images are saved uncompressed in the tagged image file format (TIFF). Due to mis-calibration of cells in digital X-ray detectors as well as impurities on the scintillator screens, stripe artifacts arose in the sinograms, which in turn generated ring artifacts in the reconstructed images.[35] Since sinogram images are not available, it is necessary to transform the images to polar coordinates, subsequently remove the vertical stripes, and transform back to Cartesian coordinates.[36] A destriping filter based on wavelet decomposition and Fourier filtering is used (highest decomposition level $L = 5$, Daubechies 30 wavelet, damping factor $\sigma = 2.0$).[37] The image stack is circularly cropped (diameter: 1600 pixels) in an automated fashion, for obtaining only the parenchyma tissue. Void and solid phase contrast is frequently not sharp; therefore, the 8-bit intensities are enhanced using contrast limited adaptive histogram equalization. The partition into void phase and material is carried out using one of the most successful variational models in image segmentation: the active contour/snake model.[38] For this purpose, a fast global minimization algorithm based on the Split-Bregman method[39] is implemented (tuning parameters: $\lambda = 10^4$, $\mu = 10^3$). Final morphological filtering eliminated redundant structures and improved the perceptibility of the void phase. The three image stacks (8-bit and binary) are cropped centrally (1130×1130 pixels), to allow better scrutiny and interpretation. 8-bit images are processed directly after the removal of ring artifacts (no contrast enhancement). The square binary (IM_B) and 8-bit (IM_G) images are used as inputs for the lacunarity and detrended fluctuation analysis, respectively.

III. THEORY AND COMPUTATIONS

A. Lacunarity

For computing lacunarity, a square structuring element or moving window of side length r is placed in the upper

left-hand corner of $IM_B \in \{0, 1\}^{M\times M}$ with $M = 1130$, such that $r \leq M$. The algorithm records the number or "mass" s of pixels that are associated with the image underneath the moving window. The window is then translated by one pixel to the right and the underlying mass is recorded again. When the moving window reaches the right-hand side of the image, it is moved back to its starting point at the left-hand side of the image, and is translated by one pixel downward. The computation proceeds until the moving window reaches the lower right-hand edge of the image, at which point it has explored every one of its $(M-r+1)^2$ possible positions. This produces a frequency distribution of box masses $n(s, r)$ (number of boxes of size r containing s occupied sites). This frequency distribution is converted into a probability distribution $Q(s, r)$ by dividing by the total number of boxes $N(r)$ of size r. The first and second moments of this distribution are determined with the following:[40]

$$Z_{(1)} = \sum_s sQ(s,r), \quad \text{and} \quad Z_{(2)} = \sum_s s^2 Q(s,r). \tag{1}$$

The statistical behavior of $\Lambda(r)$ can best be understood by recalling that[11]

$$Z_{(1)} = \mu(r) \quad \text{and} \quad Z_{(2)} = \sigma^2(r) + \mu(r)^2, \tag{2}$$

where $\mu(r)$ is the mean and $\sigma^2(r)$ is the variance of $Q(s, r)$. $\Lambda(r)$ is defined as an index of the width of $Q(s, r)$ (larger distribution width means less spatial homogeneity). Lacunarity based on the q-moments of $Q(s, r)$ is given by[41]

$$\Lambda_q(r) = \left[Z_{(2q)}/\left[Z_{(q)}\right]^2\right]^{\frac{1}{q}}, \quad \text{where} \quad Z_{(q)} = \sum_s s^q Q(s,r). \tag{3}$$

Equation (3) represents an extension of the lacunarity concept via generalized distribution moments $Z_{(q)}$, where for $q = 1$, the traditional definition is retrieved[41]

$$\Lambda(r) = Z_{(2)}/\left[Z_{(1)}\right]^2 = \left[\sigma^2(r)/\mu(r)^2\right] + 1. \tag{4}$$

The computation is repeated over a range of box sizes, ranging from $r = 1$ to some fraction of M;[11] in this case, $r \approx M/3$. Depending on the pattern, a compromise needs to be struck between larger box sizes which homogenize small-scale information but give improved statistics, and smaller box sizes which reveal finer-scale information on variation but increase statistical noise.[42] The ratio between successive box sizes is approx. $2^{1/8}$. The gliding box algorithm has the advantage of the larger sample size that leads to more robust statistical results,[43] but with edge effects—due to center oversampling and edge undersampling—observed only in strongly heterogeneous and aggregated patterns.[44] By maintaining fixed image resolutions and using the gliding box algorithm in all images, comparisons among samples are more consistent.[45] Once the computation is complete, $\Lambda(r)$ as a function of r is visualized as a double log plot. The plots explicitly characterize the spatial organization of images and measure space filling capacity in an optimal way, since any single-value index would be inadequate for characterizing complex patterns.[46] In addition, normalized lacunarity $\Lambda n(r)$ is computed from the following:[47]

$$\Lambda n(r) = 2 - \left(\frac{1}{\Lambda(r)} + \frac{1}{\Lambda c(r)}\right), \tag{5}$$

where $\Lambda c(r)$ is the complementary lacunarity (obtained by computing the lacunarity of complement IM_B). In order to validate the computational aspects of lacunarity, a range of simulated binary maps are generated, and their lacunarity curves are computed (Fig. 1). Sparse maps (images 6–9 of Fig. 1) have higher lacunarities than dense maps (images 2–5) for the same gliding box sizes. Images 2–4 that are characterized as spatially random have curves that are convex downward,[48] and exhibit a swift decay to the minimum value. In images 6–9 that have an arrangement of objects at certain scales, the curves are concave downward, while the decay is slower until the box size exceeds the scale of the objects and is rapid thereafter.[49] The generated hexa-flake fractal map (image 10) exhibits a linear monotonic decrease indicating statistical self-similarity across all scales, and rightly so because the lacunarity curve of a fractal usually displays linear behavior at a significant range of scales.[50] Note that $\Lambda(r) \geq 1$ or $\log_{10}[\Lambda(r)] \geq 0$, meaning that as $\Lambda(r) \rightarrow 1$ or $\log_{10}[\Lambda(r)] \rightarrow 0$, the image approaches a homogeneous structure. For image 1, $\log_{10}[\Lambda(r)] = 0$ due to complete lack of heterogeneity in the spatial pattern.

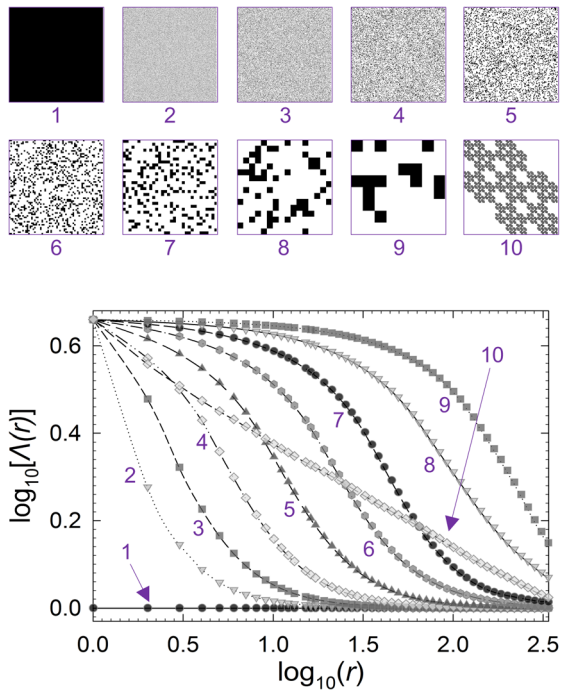

FIG. 1. Validation for computing $\Lambda(r)$ on different spatial patterns: generated maps (binary, 1024×1024 pixels, 1 per case) with zero white pixel coverage (image 1), 78.1% white pixel coverage for the deterministic hexa-flake fractal map (image 10) built recursively from smaller hexagonal patterns, and 78.1% white pixel coverage for binary maps created with a block size of 1×1 (image 2), 2×2 (image 3), 4×4 (image 4), 8×8 (image 5), 16×16 (image 6), 32×32 (image 7), 64×64 (image 8), and 128×128 pixels (image 9). Corresponding $\Lambda(r)$ curves of aforementioned maps are shown on double log scale, as a function of r.

B. Detrended fluctuation analysis

The implementation of DFA in images follows the same steps as in the one-dimensional (1D) series case. Specifically, the methodology operates on a series of pixel values $x(i)$, where $i = 1, 2, \ldots, N$ with N being the length of the series for rows (0°) and columns (90°). The sequence average and the integrated sequence obtained are given by[51]

$$x_{ave} = \frac{1}{N}\sum_{k=1}^{N} x(k) \quad \text{and} \quad y(k) = \sum_{i=1}^{k}[x(i) - x_{ave}]. \tag{6}$$

The integrated series is divided into non-overlapping segments of equal length n. In each box, a least-squares line is fitted to the data representing the trend in that box (DFA-1), thus eliminating constant trends from the original sequence or equivalently linear trends from the integrated series.[52] Next, $y(k)$ is detrended by subtracting the local trend $y_n(k)$ in each box; $y(k)$–$y_n(k)$ (fluctuation sequence). The qth order fluctuation function of this integrated and detrended series is calculated by[51]

$$F_s(n) = \left(\frac{1}{N}\sum_{k=1}^{N}[y(k) - y_n(k)]^q\right)^{\frac{1}{q}}. \tag{7}$$

Equation (7) represents the multifractal formalism of DFA, where for $q = 2$, the standard fluctuation function (monofractal DFA) is retrieved.[53] Finally, when DFA is applied to series that correspond to $IM_G \in \{0, 1, 2, \ldots, 255\}^{N\times N}$ with $N = 1130$, $F_s(n)$ is geometrically averaged over all columns/rows, respectively,[26]

$$F_{av}(n) = \left(\prod_{i=1}^{N} F_s(n)\right)^{1/N}. \tag{8}$$

Repeating this over all n, a relationship is obtained between $F_{av}(n)$ and box size n. The global scaling exponent α_G is obtained by plotting $F_{av}(n)$ against n on double log scale. The slope of the linear regression line determines α_G

$$\log_{10} F_{av}(n) = \alpha_G \log_{10} n + w, \tag{9}$$

where w is the intercept. In addition, rather than finding global scaling exponents, the use of scale-dependent scaling exponents (α_L) is also suggested.[54] For that purpose, piecewise (15 segments) cubic spline fitting with constraints is carried out in order to remove unwanted data oscillations in $F_{av}(n)$, which may have undesirable effects on α_L, followed by dF/dn for tracking the evolution of the gradient (scaling pattern) as a function of $\log_{10}(n)$. Roughly, $0.5 < \alpha < 1.0$ indicates persistent, while $0 < \alpha < 0.5$ indicates antipersistent long-range correlations.[55] Additionally, $1.0 < \alpha < 1.5$ still indicates long-range correlations but not of a power-law form, thus approaching the smoothness of Brownian noise.[56] Specifically, for $\alpha \approx 0.5$, series are uncorrelated or short-range correlated (white noise), while $\alpha \approx 1.0$ and $\alpha \approx 1.5$ correspond to pink and Brownian noise, respectively. The box sizes chosen for the computations are in the range of [4, $N \div 4$]. Smaller scales ($n < 4$) are excluded because they demonstrate transitional behavior with very high slopes.[57] For larger scales ($n > N \div 4$), $F_s(n)$ becomes statistically unreliable because the number of segments for the averaging procedure becomes very small; such deviations have been reported for DFA-1.[58] The ratio between successive box sizes is approx. $2^{1/8}$. The method is more sensitive to slowly varying trends, while quickly oscillating trends disturb the scaling behavior much less.[59] The scaling curves obtained from DFA-1 are stable over a broader range of scales.[60] Furthermore, the performance of DFA on relatively short series of synthetic and real data (i.e., 2^{10}) is deemed satisfactory for $-2 < q < 2$.[61] Here, $q = 2$ and $N = 2^{10.142}$. In order to validate DFA, simulated 8-bit coloured noise maps are generated and α values are computed (Fig. 2). The power spectral density of noise signals can be represented—as function of frequency f—by homogeneous power laws of the form $S(f) \propto 1/f^{\beta}$, where β is the spectral exponent.[62] According to the power spectral density decaying rate, three popular noises are classified as white ($\beta \approx 0$), pink ($\beta \approx 1$), and brown ($\beta \approx 2$).[63] The exponent β is related to the mean fluctuation function exponent by $\beta = 2\alpha - 1$, which holds for DFA-1.[64] The outcome for $1/f^0$, $1/f^1$, and $1/f^2$ noise maps are $\alpha = 0.510 \pm 0.03$, 0.996 ± 0.04, and 1.475 ± 0.04, respectively (mean $\pm$ σ_α).

IV. RESULTS

A. Visualization

Pore space in FH (Figs. 3(a)–3(d)) appears smaller and less heterogeneous comparing to the frozen-thawed samples (Figs. 3(e)–3(h)), illustrating the effects of freezing. The void phase areas for FH, FN1, and FN2 measured from the

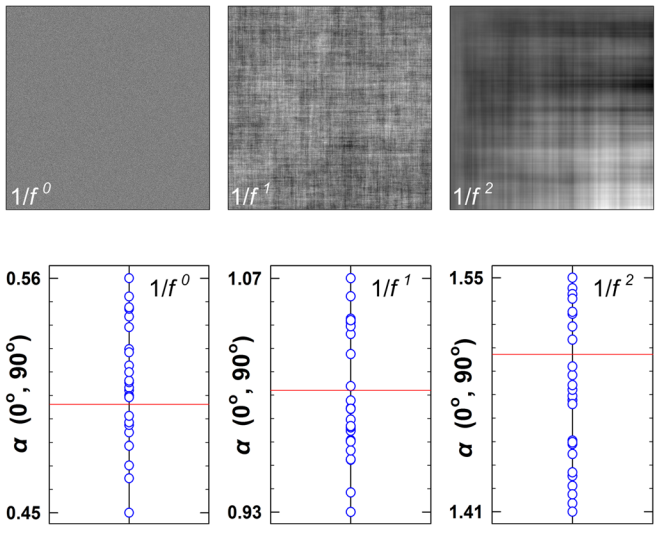

FIG. 2. Validation for computing DFA's α on different coloured noise patterns: $1/f^0$, $1/f^1$, and $1/f^2$ noise maps (8-bit, 1024×1024 pixels, 25 per case); and α values corresponding to aforementioned images. Graphs show averaged results for columns (90°) and rows (0°). The images are three samples from the generated image pool. $1/f^0$ maps are obtained from normally distributed pseudorandom numbers, $1/f^1$ maps are obtained by filtering white Gaussian signals, and $1/f^2$ maps are obtained by integrating white Gaussian noise.[62] The highlighted horizontal lines in the graphs show the expected theoretical values of α corresponding to each noise type.

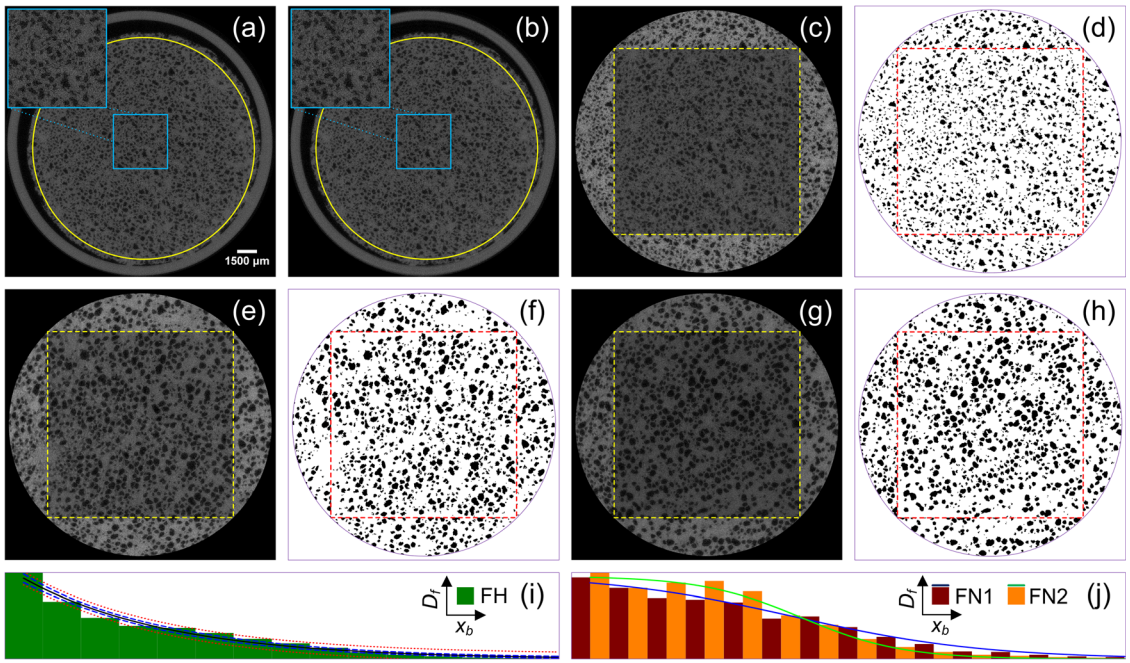

FIG. 3. Mesoscale snapshots of three cross-section samples: (a) acquired 8-bit image of fresh (FH) parenchyma; (b) same section after implementation of destriping filter for removal of ring artifacts; (c) same section circularly cropped (diameter: 1600 pixels) for obtaining the parenchyma tissue, after contrast limited adaptive histogram equalization; (d) binarized version of (c), where white and black pixels denote cellular material and pore space, respectively. Images in (e)–(h) are similar 8-bit and binary snapshots for FN1 and FN2, respectively. Magnified images in (a) and (b) demonstrate the destriping filter effect. The circular region of interest (ROI) in (a) and (b) marks parenchyma cells and pores. The square ROIs in (d), (f), and (h) mark the cropped section (1130 × 1130 pixels) for the lacunarity analysis. Similarly, the square ROIs in (c), (e), and (g) mark the same cropped section for the DFA analysis, after the removal of ring artifacts (no contrast enhancement). The Feret's diameter normalized frequency distributions of void phase, along with corresponding fits, are shown in (i) and (j) for FH and FN (FN1, FN2), respectively. The height of each rectangle in (i) and (j) indicates the normalized number of elements in the bin. The fit in (i) shows the 95% confidence and prediction bands.

circularly cropped binarized images are $A_v = 14.811 \pm 0.61\%$, $22.004 \pm 0.84\%$, and $22.560 \pm 0.75\%$, respectively (mean ± st.dev); statistical differences are observed (p-value < 0.05). Henceforth, st.dev (σ) values are obtained from the statistics of each sample cylinder or image stack. The results for FH agree with the experimentally measured effective porosity ε_e (approx. 14.2%).[65] The Feret's statistical diameter (F_d; distance between two parallel planes tangent to the pore outline) normalized frequency distributions (D_f) of the parenchyma void phase are modelled consistently best as a 3-parameter exponential decay (Fig. 3(i); $R^2 = 0.985$) and sigmoidal function (Fig. 3(j); $R^2 = 0.990$), for FH and FN, respectively,

$$D_{f(FH)} = c_3 + c_1 e^{-c_2 x_b} \quad \text{and} \quad D_{f(FN)} = c_1/(1 + e^{-((x_b - c_3)/c_2)}), \tag{10}$$

where x_b are the bins, and c_1, c_2, and c_3 are the fit coefficients. This suggest that the distributions of pore sizes are highly skewed, decreasing exponentially (FH) or sigmoidally (FN) as their size increases; number of pores inversely proportional to pore diameter.[66]

B. Spatial organization

Fig. 4(a) illustrates the scale-dependency of spatial non-stationarity using $\Lambda(r)$ as a function of r (log-log). The σ of $\log_{10}[\Lambda(r)]$ corresponding to FH, FN1, and FN2 are in the following ranges: $[2.78 \times 10^{-3}, 3.55 \times 10^{-5}]$, $[5.91 \times 10^{-3}, 9.14 \times 10^{-5}]$, and $[4.06 \times 10^{-3}, 1.01 \times 10^{-4}]$, respectively. An increasing moving window size indicates that lacunarity decreases due to the bigger level of translational invariance of the larger gliding boxes: local features become averaged. The sparser patterns of FN have higher lacunarity for the same gliding box size, which also indicates less homogeneity and greater clumping. The presence of larger pores due to freezing, in a mesostructure of smaller gaps results in larger values of lacunarity and smaller values of bulk density. Lacunarity is influenced by the variation in pore sizes in a given structure.[67] The aggregated patterns are visualized better when $\Lambda'(r)$—first derivative of $\log_{10}[\Lambda(r)]$ with respect to $\log_{10}(r)$—is plotted against box size (embedded graph in Fig. 4(a)). The curves start at a modest negative slope, decaying to the steepest slope at a break point (minima), and then increasing towards zero at larger box sizes. The trough width indicates the rate of change in object sizes over the range of measured box sizes. A narrower trough indicates discrete break points in the pattern, whereas a wider trough (FH) reveals a more continuous change in pore sizes.[68] The natural shape irregularity of the pores in FH (Fig. 3(d)) is more evident (compared to the smoother shape morphology of the FN void phase seen in Figs. 3(f) and 3(h)), and the deviation around the break point represents a more gradual change of object sizes (Fig. 3(i)).

Between $\log_{10}(r) \approx [0.85, 1.65]$, the curves decline linearly ($R^2 \approx 0.995$) (highlighted in Fig. 4(a)), which reveals statistical self-similarity in the void phase for the particular box size range,[69] indicating that intercellular air spaces are

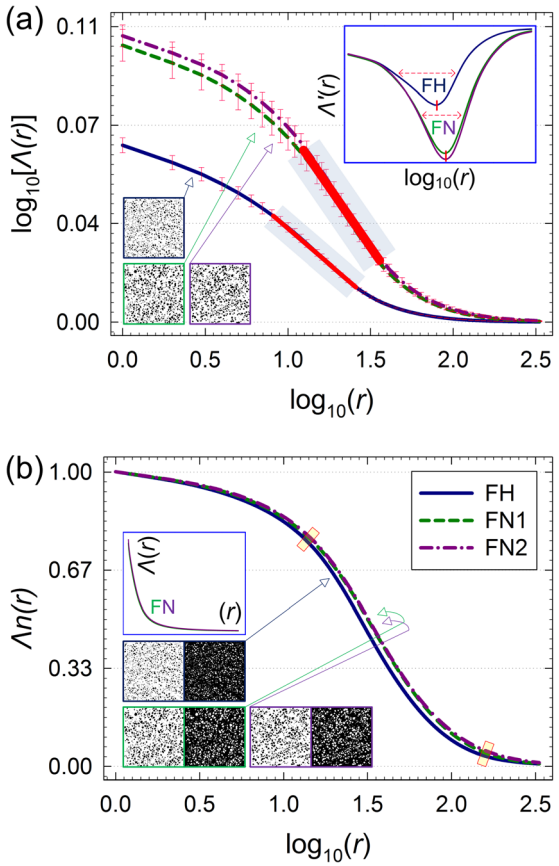

FIG. 4. Characterization of spatial heterogeneity using: (a) log-log plots with error bars of $\Lambda(r)$ (mean $\pm\, \sigma_{\Lambda(r)}$) as a function of r, and (b) log-linear plots of $\Lambda n(r)$ (mean values) as a function of r, for FH, FN1, and FN2. The embedded images in (a) and (b) are binary examples for computing $\Lambda(r)$, and their complement for computing $\Lambda c(r)$, respectively. In (a), the highlighted central sections of the curves exhibit linear monotonic decrease. The two small rectangles in (b) denote the end of lower and start of upper box size boundaries, where $\Lambda n(r)$ profiles overlap. The embedded graph in (a) illustrates $\Lambda'(r)$ as a function of $\log_{10}(r)$. The embedded graph in (b) shows the linear plot of $\Lambda(r)$ (mean) as a function of r for FN (similar profile is obtained for FH, but not shown for clarity).

organized as a fractal or multifractal objects. At increasing box sizes—mainly after $\log_{10}(r) \approx 1.75$—the profiles (Fig. 4(a)) start to converge considerably until they completely overlap, indicating that the larger gliding boxes will generally be more homogeneous,[70] thus not resolving the inherent complexities of the patterns. This might be expected because lacunarity reveals the scaling properties of patterns; a particular pattern can be discriminated from another at certain scales, while the opposite can be true at some other scales.[71] Lacunarity at smaller window sizes would measure local heterogeneity, and thus should be more sensitive to changes in the mesoscale. Variations in lacunarity profiles are observed before the size of the boxes reaches the scale of randomness of the image: $\log_{10}(r) \approx 2.00$, which is the point at which gaps appear to be almost homogeneous. For bigger box sizes (>2.00), the slope that measures the articulation of spatial structures across the pattern remains relatively unaffected.

Fig. 4(b) shows the profiles of $\Lambda n(r)$ as a function of r whose decay, within [0, 1], is a function of clustering only.[72] Since the spatial densities of FH and FN are perceptually similar (difference between averaged A_v is approx. 7%–8%), this measure is less sensitive in discerning heterogeneity. Nevertheless, some features can be assessed here as well. The curves of all mesoscale patterns are relatively similar for $\log_{10}(r) \leq 1.20$, and larger moving window sizes (≥ 2.20), but differ in the intervening range. In these intermediate box sizes, the slightly higher contagion of FN parenchyma is evident, manifesting as a spatial arrangement with relatively larger pore space sizes.[73] In essence, the variance of the void phase gap sizes within the spatial delineation of geometric objects determines the level of lacunarity.[74] The curves also exhibit slope changes and monotonic behavior in the corresponding box size ranges. When the box size reaches $\log_{10}(r) \approx 1.0$, the curve declines more slowly with increasing box size—comparing to sudden change of slope in regularly distributed and sized objects (not shown)—which is also an indication of irregularity in the void phase.[69]

From the embedded graph of Fig. 4(b)—showing the linear profiles of $\Lambda(r)$ as a function of r—it is deduced that the lacunarity function resembles a hyperbola.[75] This manifestation can be approximated using a three-parameter hyperbolic decay function ($R^2 = 0.989$)

$$\Lambda fit(r) = \left[\xi\gamma/(\gamma + r)\right] + \delta, \quad \text{where} \quad r \in [r_{\min}, r_{\max}], \quad (11)$$

where ξ, γ, and δ are the fit coefficients. This is a set of parameters that can additionally represent the variation of mass density in the images. The statistics from the implementation of the fitting are summarized in Table I. The parameters ξ and δ assume smaller mean values that differ only slightly between FH and FN, while γ assumes values within a wider numerical range and undergoes the most significant variation. A relationship can be appreciated between ξ and γ, in which a small change in ξ results to a larger one in γ. This means that γ is more sensitive to spatial organization changes in the void phase that occurs from FH to FN. Moreover, correlations exist between parameters ξ and γ, and the behavior of the lacunarity profiles with an increasing trend for both, from FH to the more lacunar FN patterns. Table I also presents the statistical dependence (r_s) between the fit parameters and A_v, assessing how well these relationships can be described using a monotonic function. Parameter ξ shows a stable strong relationship (predominantly linear with positive slope) with A_v for all samples.

TABLE I. Fit coefficients ξ, γ, and δ (mean $\pm\, \sigma$) of the three-parameter hyperbolic decay function $\Lambda fit(r)$ for FH and FN. Spearman's rank correlation coefficients (r_s) between fit parameters and A_v for FH and FN. Pairs with positive r_s tend to increase together, while for pairs with negative r_s, one variable tends to decrease, while other increases. (Different letters (g) and (h) in columns show statistical significance (p-value < 0.05)). (Symbol ** denotes significant correlations (p-value < 0.05)).

Fit parameters	ξ (mean $\pm\, \sigma_\xi$)	γ (mean $\pm\, \sigma_\gamma$)	δ (mean $\pm\, \sigma_\delta$)
FH $\Lambda fit(r)$	$0.205 \pm 0.01^{\,g}$	$7.781 \pm 0.15^{\,g}$	$0.989 \pm 0.001^{\,g}$
FN $\Lambda fit(r)$	$0.333 \pm 0.02^{\,h}$	$13.309 \pm 0.43^{\,h}$	$0.975 \pm 0.002^{\,h}$
Spearman's r_s	ξ	γ	δ
FH A_v	0.846 **	0.328 **	−0.823 **
FN A_v	0.913 **	0.669 **	−0.851 **

Parameter γ shows a weak positive correlation (FH), which becomes increasingly monotonic in FN. This verifies the sensitivity of γ to the freezing-induced changes that lead to higher contagion, while δ shows consistent strong negative correlations.

C. Correlation properties

Fig. 5(a) presents a double log plot of $F_{av}(n)$ as a function of n, averaged for 0° and 90° image orientations. DFA avoids the spurious detection of correlations that are artifacts of non-stationarities.[76] Non-stationarities can appear in series due to segments removed caused by discontinuities, appearance of random spikes, and different local behaviors.[77] The KPSS statistic (significance at 5% level) verifies the non-stationarity of all rows and columns forming the images of the parenchyma tissue samples. Non-stationarity can be visualized from the appearance of the embedded line profile in Fig. 5(b), showing a behavior similar to heartbeat dynamics.[78] This is more or less expected due to the topography of the greyscale intensities

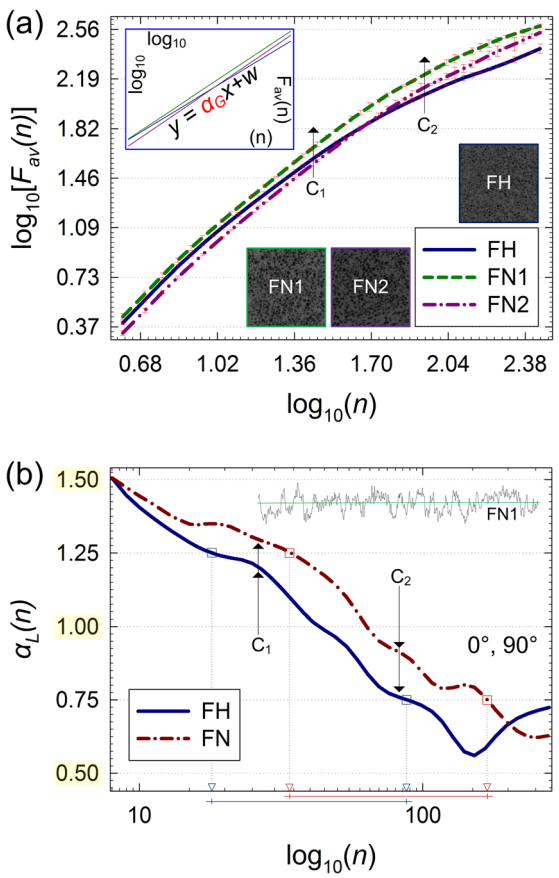

FIG. 5. Characterization of correlation properties using: (a) log-log plots with error bars of $F_{av}(n)$ (mean $\pm\, \sigma_{F(n)}$) as a function of n for FH, FN1, and FN2, and (b) log-linear plots of scale-dependent $\alpha_L(n)$ (mean values) as a function of n, for the FH and FN parenchyma tissue. In (a) and (b), the curves show averaged results for columns (90°) and rows (0°). The embedded images in (a) are 8-bit examples for computing $F_{av}(n)$. The embedded graph in (a) illustrates the linear fitting from Eq. (9) for all patterns ($R^2 > 0.969$). In (a) and (b), C_1 and C_2, show the crossover positions to different correlation regimes at different spatial scales. The highlighted values on the y-axis in (b) show the values of α corresponding to $1/f^0$, $1/f^1$, and $1/f^2$ noise. In (b), a sequence of greyscale intensities corresponding to an image from the FN1 stack at $N/2$ and 90° is visualized as a line profile. The scale ranges (x-axis) in which $\alpha_L = [1.25, 0.75]$ are shown in (b) for FH and FN.

landscape.[26] The variability between the results of Fig. 5(a) for rows and columns is not substantial ($\sigma_{min} = 1.09 \times 10^{-5}$, $\sigma_{max} = 0.038$). The σ of $\log_{10}[F_{av}(n)]$ corresponding to FH, FN1, and FN2 are in the following ranges: [0.024, 0.091], [0.023, 0.084], and [0.021, 0.092], respectively. The embedded graph in (a) illustrates the linear fitting—using Eq. (9)—for all patterns ($R^2 > 0.969$). The results of the linear fitting are $\alpha_G = 1.029 \pm 0.04$ and 1.091 ± 0.03, for FH and FN, respectively, (mean $\pm\, \sigma_\alpha$). The strongly persistent nature of the long-range correlations in the parenchyma can be explained from the textural content of the images: pixel values corresponding to either cellular material or pore space are approx. equally correlated with preceding pixels and pixels prior to that.[79] Usually, long-range correlations are a result of collective behavior, with multiple components interrelating through local interactions.[80] The disruption of the meso-architecture from the formation of ice crystals is not substantial, and as expected does not induce anti-correlation properties over different scales.

It is typical that the root-mean-square fluctuations as a function of box sizes shown in Fig. 5(a) are not strictly linear but rather consist of distinct regions of different slopes separated at crossover points, like in the case of complex physiological signals.[81] This suggests that there are short- and long-range scaling exponents that characterize the correlation properties.[82] FH and FN exhibit fairly similar crossover patterns at $\log_{10}(n)$: $C_1 = 1.43$ (27 pixels), and $C_2 = 1.92$ (83 pixels). These crossovers indicate a transition from one type to a different type of underlying correlation at smaller, intermediate, and larger spatial scales.[83] The progression in the values of α_C exponents in the three corresponding segments is $1.413 \rightarrow 0.952 \rightarrow 0.641$ ($R^2 > 0.996$), and $1.458 \rightarrow 1.119 \rightarrow 0.743$ ($R^2 > 0.997$), for FH and FN, respectively. At smaller scales, $\alpha_C \approx 1.5$ indicates that the parenchyma mesoscale resembles $1/f^2$ noise, whereas for larger scales, the data exhibit long-range correlations ($\alpha_C \approx 0.7$). The latter is more prevalent, which explains the average scaling behavior (α_G) around $1/f^1$ noise.

From the definition of DFA, the scaling exponents can be viewed as indicators of "visual roughness" of the intensity sequences; i.e., larger scaling exponent reflects slower fluctuations.[84] The α_C exponents for FN decrease at smaller rate than in FH, which is mainly due to more frequent presence of larger intercellular spaces (Figs. 3(e) and 3(g)). However, in the mesostructure of FH, the natural arrangement of cells and voids is translated to the more rapid fluctuations of the greyscale intensities (Fig. 3(c)). This explains the lower values of α_C in the larger spatial scales (FH). Additionally, while for FN, the transition in C_2 is essentially a change from strong to weak persistence; for FH, this is more pronounced and the visual texture seems to move towards short-range correlations.

While common practice is to focus on the raw fluctuation plots with defined regimes of scaling behavior, the use of scale-dependent scaling exponents reveals more information. Fig. 5(b) illustrates the behavior of the gradient (α_L) of the root-mean-square fluctuations as a function of $\log_{10}(n)$. The x-axis starts at the scale of 8 pixels; since for $n < 8$, the α_L values for FH and FN are nearly identical. A general

observation is that for all samples, α_L decreased as a function of the length scale, from a Brownian-like motion behavior in the small-scale range to a less ordered parenchyma, with increasing n.[26] The scaling pattern of local exponents verifies the slower fluctuations (in comparison to FH) induced by freezing for scales up to approx. 150 pixels. In the scale range $n_{FH} = [18, 89]$ and $n_{FN} = [34, 167]$ pixels, which corresponds to $\alpha_L = [1.25, 0.75]$, both FH and FN decay monotonically, showing persistent long-range correlations that affect the statistics of α_G. Since $n_{FN} > n_{FH}$, the average behavior around $1/f^1$ noise is more characteristic for FN. As a result, the single α_G exponent may characterize the data globally in the intermediate to long-term range. For spatial scales > 100 pixels, the α_L for FH do not decrease monotonically and a global minimum is observed around 150 pixels, where the less correlated behavior is found; this is close to 0.5, where any future predictions of the sequence are impossible.[85] This could be rationalized from the apparent natural anisotropic (and almost stochastic for the particular scale) visual texture of FH. This is the second salient feature of Fig. 5(b), which is not observed in FN. This signifies that the scaling pattern of FH depends more strongly on the region, and that α_G is not as representative as in the FN case. For scales >150 pixels, the α_L values for FH increase and this indicates that larger spatial scales resolve a more ordered mesostructure.[86] This also suggests power-law long-range correlations; when correlations decay with a power-law form, on average the system is scale-free because there is no characteristic scale associated with a power law.[87] This scale invariance of the spatial patterns of image intensities indicates an analogy to the statistical mechanics of physical systems at a critical point.[88]

V. DISCUSSION

Freezing imparted a relatively altered spatial arrangement of the pore space. This is verified by the sigmoidal shape of the intercellular air spaces distribution (Fig. 3(j)) in FN, which indicates the more frequent occurrence of larger pores comparing to the gradual decrease in pore diameter for FH. Parenchymatous tissue with greater fractional air volumes can be texturally softer and has greater internal gas diffusion rates.[89,90] The mesostructural landscape in FN is collectively caused by the permanent transfer of intracellular H_2O to the extracellular environment, and the cell rupture. The manifestation of these structural alterations in the visual texture of the images is mainly an amalgam of characteristics that include the variation of pixel tone, and the emergence of surface patterns.

The statistical self-similarity, seen in Fig. 4, implies that a fairly similar morphology is evident in the designated range, or more precisely statistical measures are preserved across the studied scales. The fractality of the void phase in FH for the particular box size ranges can be understood by considering the mechanisms that led to its formation.[91] A fractal structure is often the one that best reconciles the microscopic organisation laws and the macroscopic constraints.[92] In apple fruit growth, this may correspond to: (i) cell proliferation and expansion[93,94] with enlargement of air gaps between cells[4] and (ii) physiological conditions. The development of pore spaces involves the replacement of cells with no intercellular spaces with: (i) cells interspersed with intercellular spaces by the extensive separation of the middle lamellae (schizogenous spaces), and (ii) cells interspersed with dead cells whose contents and walls are lysed (lysigenous spaces).[95] The majority of the voids in apple cortex have large polygonal concave cross sections, indicating a lysigenous origin.[5] Self-similarity is more pronounced after the freezing-thawing cycle that signifies fractality as an intrinsic mesoscale feature of FN parenchyma. Due to vacuole rupture, the interaction between cell walls and contents is facilitated allowing cell wall enzymatic dissolution during thawing.[96] Modification of pectins and hemicelluloses contributes to cell wall collapse resulting in cell separation with the presence of larger intercellular spaces (Figs. 3(f) and 3(h)).

Fig. 5 indicates an average behavior around flicker ($1/f^1$) noise, which can be interpreted as a compromise between the unpredictability of white noise and the smoother landscape of Brownian noise,[84] suggesting long-range correlations in parenchyma visual texture. The emergence of the observed properties for FH may derive from modular growth mechanisms[97] that result in the hierarchical arrangement of the parenchyma tissue; equiaxed, polyhedral cells densely packed together that from a topological standpoint can be modelled as closed-cell foams.[2] From a genetics perspective, this can be attributed to the homologous SEPALLATA1/2-like genes MADS8 and MADS9 that control the development of discrete zones within the hypanthium tissue (from which apple flesh develops), therefore regulating flesh formation.[98] Macroscopically, these subtleties are manifested as growth patterns that can be typified using expolinear, Gompertz, and logistic models.[99] The actual growth process is typically a non-deterministic process, partly because it is influenced continuously by the environment, e.g., supply of nutrients and because growth is limited by geometric restrictions.[100] Regarding FN, the freezing-thawing cycle made the correlation properties around $1/f^1$ noise to be a salient mesoscale feature of change in the arrangement and size of parenchymatous voids.

VI. CONCLUSIONS AND FURTHER WORK

Disordered multiphase media, ranging from porous materials to biological tissues, are ubiquitous and their understanding is of fundamental importance.[101] The extension of spatial analysis and statistical physics methods in plant tissue systems is certainly both inspiring and challenging. The structure of intercellular air spaces plays an important role on mechanical properties and the governing fluid and gas transport mechanisms. The architectural complexity of intercellular air spaces makes single geometrical measurements insufficient to characterize the heterogeneity of the pore space. The inhomogeneity of distribution depends not only on the percentage content of phase, but also on how the phase fills the space.[102] The lacunarity morphometric, as a multiscale measure of binary texture, provides information about the distribution of gaps that correspond to the degree

of spatial heterogeneity in the parenchyma tissue. Similarly, modern theories have suggested strategies, where the focus has shifted from the study of averages and histograms to the study of patterns in data fluctuations.[103] The usefulness of DFA is that of providing insights on the correlation properties of the parenchyma at different spatial scales. Overall, complex systems methods lead to better insights regarding the freezing-induced modifications upon the arrangement of cells and voids, and can further stimulate interest for the analysis of internal plant tissue structures coupled with other physico-chemical processes or phenomena.

Surely, the effects of low temperature environments on the micro- and meso-architectural arrangement and integrity of plant tissue, merit further investigation. Other examples, where complex systems approaches could provide an elaborate analysis framework includes the assessment of: tissue development during growth, dynamic processes (e.g., ripening and senescence), physiological disorders, postharvest biotic, abiotic stress, etc. Data from the internal structure of plant tissues could be acquired from other imaging modalities as well. In addition, it can be intriguing to see how similar approaches can be used to offer further insights. Quantifying the intrinsic geometrical properties of complex spatial patterns allows the construction of statistical models that may correlate with structural, mechanical, physiological, or other properties. Multilacunarity analysis[41] could reveal additional features that correspond to the spatial organization of the tissue. Aggregation patterns could be analyzed with a generalized index that indicates whether spatial datasets are at a complete spatial randomness state.[104] Mathematical equivalence for α calculated by DFA and by an alternative method using frequency-weighted power spectra has been demonstrated.[105] The latter approach would be an interesting comparison. In addition, for data that are multifractal (non-Gaussian fluctuations or nonlinear correlations) characterization requires either two or more values of α or a continuous spectrum $f(\alpha)$.[106] Multifractal DFA and its two-dimensional generalization[107] may provide subtler indices for assessing structural modifications in the tissue. As an additional example, the visibility graph method[108] may also offer a different point of view in analysing 1D series from mesoscale snapshots. In this experiment, the analyses on the 2D sections proved quite effective in providing relevant and quantitative information. The approach avoided the methodological and computational complexities arising from techniques that work on the 3D structure of the parenchymatous tissue pore network.[109,110] However, the 3D characteristics of such mesostructures could be studied as well with properly adapted algorithms[107,108,111] or novel indices of interest.

[1]L. Dražeta, A. Lang, A. J. Hall, R. K. Volz, and P. E. Jameson, J. Exp. Bot. **55**, 1061 (2004).
[2]L. J. Gibson, J. R. Soc., Interface **9**, 2749 (2012).
[3]J. Cybulska, A. Zdunek, K. M. Psonka-Antonczyk, and B. T. Stokke, Carbohydr. Polym. **92**, 128 (2013).
[4]P. A. McAtee, I. C. Hallett, J. W. Johnston, and R. J. Schaffer, Plant Methods **5**, 5 (2009).
[5]P. Verboven, G. Kerckhofs, H. K. Mebatsion, Q. T. Ho, K. Temst, M. Wevers, P. Cloetens, and B. M. Nicolaï, Plant Physiol. **147**, 518 (2008).
[6]R. F. Evert, *Esau's Plant Anatomy* (John Wiley & Sons, Hoboken, 2006), pp. 175–190.
[7]Q. T. Ho, P. Verboven, S. W. Fanta, M. K. Abera, M. A. Retta, E. Herremans, T. Defraeye, and B. M. Nicolaï, Food Bioprocess Technol. **7**, 482 (2014).
[8]A. A. Khan and J. F. V. Vincent, J. Sci. Food Agric. **52**, 455 (1990).
[9]R. Mizutani and Y. Suzuki, Micron **43**, 104 (2012).
[10]V. J. L. Ting, P. Silcock, P. J. Bremer, and F. Biasioli, J. Food Sci. **78**, E1735 (2013).
[11]R. E. Plotnick, R. H. Gardner, W. W. Hargrove, K. Prestegaard, and M. Perlmutter, Phys. Rev. E **53**, 5461 (1996).
[12]K. Uno, J. Uozumi, and T. Asakura, Wave Random Complex Media **5**, 253 (1995).
[13]L. Da Fontoura Costa, F. Rocha, and S. M. A. De Lima, Appl. Phys. Lett. **86**, 093901 (2005).
[14]E. P. Rodrigues, M. S. Barbosa, and L. F. Costa, Phys. Rev. E **72**, 016707 (2005).
[15]P. Dong, Int. J. Remote Sens. **21**, 3369 (2000).
[16]C. R. Tolle, T. R. McJunkin, and D. J. Gorsich, Physica D **237**, 306 (2008).
[17]R. H. C. Melo, E. A. Vieira, and A. Conci, *in Characterizing the Lacunarity of Objects and Image Sets and Its Use as a Technique for the Analysis of Textural Patterns*, edited by J. Blanc-Talon, W. Philips, W. Popescu, and P. Scheunders (Springer-Verlag, Berlin, 2006), pp. 208–219.
[18]M. R. T. Dale, P. Dixon, M. J. Fortin, P. Legendre, D. E. Myers, and M. S. Rosenberg, Ecography **25**, 558 (2002).
[19]Q. Cheng, Math. Geol. **29**, 919 (1997).
[20]R. A. Feagin, Physica A **328**, 315 (2003).
[21]J. B. Gao, Y. H. Cao, W. W. Tung, and J. Hu, *Multiscale Analysis of Complex Time Series* (Wiley Interscience, Hoboken, 2007), pp. 79–151.
[22]P. Grau-Carles, Physica A **360**, 89 (2006).
[23]F. Biagini, Y. Hu, B. Øksendal, and T. Zhang, *Stochastic Calculus for Fractional Brownian Motion and Applications* (Springer-Verlag, London, 2008), pp. 5–22.
[24]M. Martini, A. Knežević, G. Krstačić, and E. Vargović, Phys. Rev. E **70**, 012903 (2004).
[25]M. Shelhamer, *Nonlinear Dynamics in Physiology: State-Space Approach* (World Scientific Publishing, New Jersey, 2006), pp. 211–219.
[26]J. Alvarez-Ramirez, E. Rodriguez, I. Cervantes, and J. C. Echeverria, Physica A **361**, 677 (2006).
[27]C. K. Peng, S. V. Buldyrev, S. Havlin, M. Simons, H. E. Stanley, and A. E. Goldberger, Phys. Rev. E **49**, 1685 (1994).
[28]A. J. Einstein, H. S. Wu, and J. Gil, Fractals **10**, 19 (2002).
[29]Z. Chen, E. N. Brown, and R. Barbieri, IEEE Trans. Biomed. Eng. **57**, 1335 (2010).
[30]A. E. Delgado, L. Zheng, and D. W. Sun, Food Bioprocess Technol. **2**, 263 (2009).
[31]H. C. Chun, D. Giménez, and S. W. Yoon, Geoderma **146**, 83 (2008).
[32]C. K. Peng, S. Havlin, H. E. Stanley, and A. L. Goldberger, Chaos **5**, 82 (1995).
[33]P. Lancaster and K. Šalkauskas, *Curve and Surface Fitting: An Introduction* (Academic Press, London, 1986), pp. 67–112.
[34]D. Kwiatkowski, P. C. B. Phillips, P. Schmidt, and Y. Shin, J. Econ. **54**, 159 (1992).
[35]E. M. A. Anas, S. Y. Lee, and M. K. Hasan, Phys. Med. Biol. **55**, 6911 (2010).
[36]M. J. Blunt, B. Bijeljic, H. Dong, O. Gharbi, S. Iglauer, P. Mostaghimi, A. Paluszny, and C. Pentland, Adv. Water Resour. **51**, 197 (2013).
[37]B. Münch, P. Trtik, F. Marone, and M. Stampanoni, Opt. Express **17**, 8567 (2009).
[38]X. Bresson, S. Esedoglu, P. Vandergheynst, J. P. Thiran, and S. Osher, J. Math. Imaging Vision **28**, 151 (2007).
[39]T. Goldstein, X. Bresson, and S. Osher, J. Sci. Comput. **45**, 272 (2010).
[40]R. E. Plotnick, R. H. Gardner, and R. V. O'Neill, Landscape Ecol. **8**, 201 (1993).
[41]J. Vernon-Carter, C. Lobato-Calleros, R. Escarela-Perez, E. Rodriguez, and J. Alvarez-Ramirez, Physica A **388**, 4305 (2009).
[42]Y. Malhi and R. M. Román-Cuesta, Remote Sens. Environ. **112**, 2074 (2008).
[43]A. Saa, G. Gascó, J. B. Grau, J. M. Antón, and A. M. Tarquis, Nonlinear Processes Geophys. **14**, 603 (2007).
[44]R. A. Feagin, X. B. Wu, and T. Feagin, Ecol. Modell. **201**, 262 (2007).
[45]D. E. Pendleton, A. Dathe, and P. Baveye, Phys. Rev. E **72**, 041306 (2005).
[46]P. Dong and B. Leblon, Int. J. Remote Sens. **25**, 3745 (2004).

[47]G. Dougherty and G. M. Henebry, Med. Eng. Phys. **23**, 369 (2001).
[48]M. R. T. Dale, Landscape Ecol. **15**, 467 (2000).
[49]G. M. Henebry and H. J. H. Kux, Int. J. Remote Sens. **16**, 565 (1995).
[50]C. Allain and M. Cloitre, Phys. Rev. A **44**, 3552 (1991).
[51]L. Telesca and V. Lapenna, *Fractal Methods in Self-Potential Signals Measured in Seismic Areas*, edited by V. Dimri (Springer-Verlag, Berlin, 2005), pp. 133–178.
[52]P. C. Ivanov, *Long-Range Dependence in Heartbeat Dynamics*, edited by G. Rangarajan and M. Ding (Springer-Verlag, Berlin, 2004), pp. 339–372.
[53]J. W. Kantelhardt, S. A. Zschiegner, E. Koscielny-Bunde, S. Havlin, A. Bunde, and H. E. Stanley, Physica A **316**, 87 (2002).
[54]J. C. Echeverría, M. S. Woolfson, J. A. Crowe, B. R. Hayes-Gill, G. D. Croaker, and H. Vyas, Chaos **13**, 467 (2003).
[55]L. Telesca and M. Macchiato, Chaos, Solitons Fractals **19**, 377 (2004).
[56]R. Yan, G. Yan, W. Zhang, and L. Wang, Commun. Nonlinear Sci. Numer. Simul. **13**, 1888 (2008).
[57]J. Zhu and Z. Liu, Atmos. Environ. **37**, 2605 (2003).
[58]A. Bashan, R. Bartsch, J. W. Kantelhardt, and S. Havlin, Physica A **387**, 5080 (2008).
[59]J. W. Kantelhardt, E. Koscielny-Bunde, H. A. H. Rego, S. Havlin, and A. Bunde, Physica A **295**, 441 (2001).
[60]L. Xu, P. C. Ivanov, K. Hu, Z. Chen, A. Carbone, and H. E. Stanley, Phys. Rev. E **71**, 051101 (2005).
[61]J. L. López and J. G. Contreras, Phys. Rev. E **87**, 022918 (2013).
[62]M. R. Schroeder, *Fractals, Chaos, Power Laws: Minutes from an Infinite Paradise* (Freeman & Company, New York, 1991), pp. 121–138.
[63]L. Zão and R. Coelho, IEEE Signal Process. Lett. **18**, 675 (2011).
[64]Y. Zhou, Y. Leung, and Z. G. Yu, Phys. Rev. E **87**, 012921 (2013).
[65]J. M. Del Valle, V. Aránguiz, and L. Díaz, J. Food Eng. **38**, 207 (1998).
[66]W. M. Edwards, L. D. Norton, and C. E. Redmond, Soil Sci. Soc. Am. J. **52**, 483 (1988).
[67]M. N'Diaye, C. Degeratu, J. M. Bouler, and D. Chappar, Mater. Sci. Eng., C **33**, 2025 (2013).
[68]C. R. Butson and D. J. King, Int. J. Remote Sens. **27**, 105 (2006).
[69]N. Marwan, P. Saparin, and J. Kurths, Eur. Phys. J. Spec. Top. **143**, 109 (2007).
[70]G. D. Du and T. S. Yeo, IEEE Trans. Geosci. Remote Sens. **40**, 980 (2002).
[71]P. Dong, Ann. GIS **6**, 20 (2000).
[72]D. C. Manikka-Baduge and G. Dougherty, Proc. SPIE **7259**, 725953 (2009).
[73]S. W. Myint and N. Lam, Comput. Environ. Urban Syst. **29**, 501 (2005).
[74]S. W. Myint, V. Mesev, and N. Lam, Geogr. Anal. **38**, 371 (2006).
[75]A. Zaia, R. Eleonor, P. Maponi, R. Rossi, and R. Murri, IEEE Trans. Inf. Technol. Biomed. **10**, 484 (2006).
[76]P. Shang, Y. Lu, and S. Kamae, Chaos, Solitons Fractals **36**, 82 (2008).
[77]C. V. Chianca, A. Ticona, and T. J. P. Penna, Physica A **357**, 447 (2005).
[78]H. E. Stanley, L. A. N. Amaral, A. L. Goldberger, S. Havlin, P. C. Ivanov, and C. K. Peng, Physica A **270**, 309 (1999).
[79]M. S. Keshner, Proc. IEEE **70**, 212 (1982).
[80]M. V. José and R. F. Bishop, Philos. Trans. R. Soc. London, Ser. B **358**, 1625 (2003).
[81]R. U. Acharya, C. M. Lim, and P. Joseph, ITBM-RBM News **23**, 333 (2002).
[82]J. Yue, X. Zhao, and P. Shang, Math. Probl. Eng. **2010**, 749894 (2010).
[83]Z. Chen, P. C. Ivanov, K. Hu, and H. E. Stanley, Phys. Rev. E **65**, 041107 (2002).
[84]S. Leistedt, M. Dumont, J. P. Lanquart, F. Jurysta, and P. Linkowski, Clin. Neurophysiol. **118**, 940 (2007).
[85]P. A. Varotsos, N. V. Sarlis, and E. S. Skordas, Phys. Rev. E **66**, 011902 (2002).
[86]C. Lobato-Calleros, E. Rodriguez, O. Sandoval-Castilla, E. J. Vernon-Carter, and J. Alvarez-Ramirez, Food Res. Int. **39**, 678 (2006).
[87]P. C. Ivanov, L. A. Nunes Amaral, A. L. Goldberger, S. Havlin, M. G. Rosenblum, H. E. Stanley, and Z. R. Struzik, Chaos **11**, 641 (2001).
[88]G. J. Stephens, T. Mora, G. Tkačik, and W. Bialek, Phys. Rev. Lett. **110**, 018701 (2013).
[89]R. K. Volz, F. R. Harker, I. C. Hallet, and A. Lang, *Development of Texture in Apple Fruit – A Biophysical Perspective*, Vol. 636, edited by A. D. Webster (ISHS Acta Horticulturae, Toronto, 2004), pp. 473–479.
[90]Q. T. Ho, B. E. Verlinden, P. Verboven, S. Vandewalle, and B. M. Nicolaï, J. Exp. Bot. **57**, 4215 (2006).
[91]J. B. Bassingthwaighte, L. S. Liebovitch, and B. J. West, *Fractal Physiology* (Oxford University Press, New York, 1994), pp. 285–299.
[92]A. Lesne and M. Laguës, *Scale Invariance: From Phase Transitions to Turbulence* (Springer, Berlin, 2003), pp. 43–54.
[93]J. E. Jackson, *Biology of Apples and Pears* (Cambridge University Press, Cambridge, 2003), pp. 268–340.
[94]A. Malladi and P. M. Hirst, J. Exp. Bot. **61**, 3003 (2010).
[95]J. A. Raven, Ann. Bot. **78**, 137 (1996).
[96]S. Chassagne-Berces, C. Poirier, M. D. Devaux, F. Fonseca, F. Lahaye, G. Pigorini, C. Girault, M. Marin, and F. Guillon, Food Res. Int. **42**, 788 (2009).
[97]L. Dražeta, A. Lang, A. J. Hall, R. K. Volz, and P. E. Jameson, J. Hortic. Sci. Biotechnol. **79**, 241 (2004).
[98]H. S. Ireland, J. L. Yao, S. Tomes, P. W. Sutherland, N. Nieuwenhuizen, K. Gunaseelan, R. A. Winz, K. M. David, and R. J. Schaffer, Plant J. **73**, 1044 (2013).
[99]I. J. Warrington, T. A. Fulton, E. A. Halligan, and H. N. De Silva, J. Am. Soc. Hortic. Sci. **124**, 468 (1999).
[100]J. A. Kaandorp, *Fractal Modelling: Growth and Form in Biology* (Springer-Verlag, Berlin, 1994), pp. 7–54.
[101]P. Tahmasebi and M. Sahim, Phys. Rev. Lett. **110**, 078002 (2013).
[102]J. Chmiela, D. Słota, and J. Szala, Mater. Charact. **56**, 421 (2006).
[103]A. Paraschiv-Ionescu and K. Aminian, *Nonlinear Analysis of Physiological Time Series*, edited by A. Naït-Ali (Springer, Berlin, 2009), pp. 307–333.
[104]E. J. Hackett-Jones, K. J. Davies, B. J. Binder, and K. A. Landman, Phys. Rev. E **85**, 061908 (2012).
[105]K. Wilson, D. P. Francis, R. Wensel, A. J. S. Coats, and K. H. Parker, Physiol. Meas. **23**, 385 (2002).
[106]P. Oświęcimka, J. Kwapień, and S. Drożdż, Phys. Rev. E **74**, 016103 (2006).
[107]G. F. Gu and W. X. Zhou, Phys. Rev. E **74**, 061104 (2006).
[108]L. Lacasa, B. Luque, F. Ballesteros, J. Luque, and J. C. Nuño, Proc. Natl. Acad. Sci. U.S.A. **105**, 4972 (2008).
[109]M. K. Abera, S. W. Fanta, P. Verboven, Q. T. Ho, J. Carmeliet, and B. M. Nicolai, Food Bioprocess Technol. **6**, 859 (2013).
[110]M. K. Abera, P. Verboven, E. Herremans, T. Defraeye, S. W. Fanta, Q. T. Ho, J. Carmeliet, and B. M. Nicolai, Food Bioprocess Technol. **7**, 542 (2014).
[111]P. Dong, Comput. Geosci. **35**, 2100 (2009).
[112]H. Kiani, Z. Zhang, A. Delgado, and D.-W. Sun, Food Res. Int. **44**(9), 2915–2921 (2011).
[113]L. Y. Zheng and D.-W. Sun, Trends Food Sci. Technol. **17**(1), 16–23 (2006) .
[114]D.-W. Sun and B. Li, J. Food Eng. **57**(4), 337–345 (2003).
[115]B. Li and D.-W. Sun, J. Food Eng. **55**(3), 277–282 (2002).
[116]D.-W. Sun and T. Brosnan, Int. J. Refrig.-Rev. Int. Du Froid **22**(6), 472–478 1999.
[117]D.-W. Sun and L. Y. Zheng, J. Food Eng. **77**(2), 203–214 2006.
[118]D.-W. Sun and Z. H. Hu, Int. J. Refrig.-Rev. Int. Du Froid **26**(1), 19–27 2003.
[119]L. J. Wang and D.-W. Sun, Trends Food Sci. Technol. **12**(5–6), 174–184 2001.
[120]D.-W. Sun and J. L. Woods, Drying Technol. **11**(7), 1523–1551 (1993); D.-W. Sun and J. L. Woods, Trans. ASAE **37**(6), 1919–1926 (1994a); D.-W. Sun and J. L. Woods, J. Agric. Eng. Res. **59**(4), 273–283 (1994b); D.-W. Sun and J. L. Woods, Drying Technol. **15**(10), 2479–2508 (1997).
[121]Z. W. Cui, S. Y. Xu, and D.-W. Sun, Drying Technol. **22**(3), 563–575 (2004).
[122]D.-W. Sun and C. Byrne, J. Agric. Eng. Res. **69**(4), 307–315 (1998).
[123]D.-W. Sun, J. Stored Prod. Res. **35**(3), 249–264 (1999).
[124]A. E. Delgado and D.-W. Sun, J. Food Eng. **51**(2), 163–170 (2002).
[125]S. Y. Xu, X. F. Chen, and D.-W. Sun, J. Food Eng. **50**(4), 211–216 (2001).